Transient Oscillation Suppression Method of Modular Multilevel DC Transformer

DAN LYU[1], **(Graduate Student Member, IEEE), YICHAO SUN**[1,2], **(Member, IEEE),**
YUFAN LI[1], **JIANFENG ZHAO**[2], **ZHENDONG JI**[3], **AND DONGYE LI**[4], **(Member, IEEE)**

[1]School of Electrical and Automation Engineering, Nanjing Normal University, Nanjing 210023, China
[2]Jiangsu Provincial Key Laboratory of Smart Grid Technology and Equipment, Southeast University, Nanjing 210096, China
[3]School of Automation, Nanjing University of Science and Technology, Nanjing 210094, China
[4]School of Electric Power Engineering, Nanjing Institute of Technology, Nanjing 211167, China

Corresponding author: Yichao Sun (yichao.sun1987@gmail.com)

ABSTRACT The modular multilevel DC transformer (MMDCT) is more likely to suffer from transient oscillation, which is caused by insufficient damping of the equivalent *RLC* circuit with smaller arm resistance and submodule capacitance and may threaten the system stability. To tackle this issue, this paper conducts an in-depth analysis of the oscillation generating mechanism and thereby proposes a transient oscillation suppression method by incorporating an oscillation suppression angle (OSA) between the upper and lower arm switching voltages, with which the direction of the circulating current could be adjusted during this overlapped period. However, the open loop control of OSA shows indistinctive improvement of the damping ratio so that a damping compensator for regulating the circulating current is utilized. Furthermore, the compensating gain is optimally designed to achieve the critical damping state based on the small-signal model viewing OSA as an input variable. Besides, the outer capacitor voltage control loop and the power control loop are incorporated to provide the circulating current reference and to track the load power demand, respectively. Extensive simulation results from a realistically designed MMDCT model in PSIM validate the feasibility and effectiveness of the proposed transient oscillation suppression method.

INDEX TERMS Modular multilevel DC transformer, damping compensation, oscillation suppression, inter-arm phase shift angle, controller design.

I. INTRODUCTION

As the concept of sustainable development is deeply rooted in people's minds, the development and utilization of renewable energy represented by hydropower, wind energy and solar energy has become a hot topic worldwide. However, due to the inherent intermittent nature of renewable energy resources, high penetration of renewable energy sources poses serious challenges to the stable operation of existing power systems. On the contrary, the DC power grid is considered to be a preferable way for renewable energy access in the future because it does not require reactive power compensation and frequency synchronization [1]. Therefore, as the

The associate editor coordinating the review of this manuscript and approving it for publication was Xiaorong Xie.

core component of the DC power grid, DC transformers have received more and more attention in recent years [2].

A typical DC transformer is the dual active bridge (DAB) structure [3], [4], which realizes the bidirectional power flow by properly applying voltage across the leakage inductance of the medium-frequency transformer. Furthermore, the conflict between the low voltage stress of commercial power semiconductor devices and high voltage rating of the power grid is preferably managed by using multilevel concepts. Due to the expansibility and flexibility of the modular multilevel converter (MMC) [5]–[9], a modular multilevel DC transformer (MMDCT) based on half bridge submodule (SM) is proposed in [10], [11].

A majority of papers [12]–[19] have cast attention to the common problem of the DC transformers, such as soft switching characteristics, current stress and efficiency optimization

to improve reliability and stability based on the square wave modulation scheme. Nevertheless, the issues unique to MMDCT are more worthy of in-depth study.

To be specific, the series connected structure of submodule capacitors, the arm inductor along with its parasitic resistor is liable to suffer from *RLC* resonance issue, which also occurs in some PWM controlled grid-connected circuits such as current/voltage source rectifier [21]–[25], indirect matrix converter [26] and voltage source motor drives [27], [28], with the *LC* filter incorporated to alleviate the harmonic distortion at the input side. Hence the associated transient oscillation will be excited in the *LC* filter by the outer transient disturbances and the grid voltage harmonics. The damping resistors physically existed within the *LC* elements does help to increase the damping ratio, but it is preferred to be avoided due to the unexpected power losses [28], especially in high power applications. On the other hand, the approach of using active damping to suppress the *LC* oscillation has been investigated and can be categorized into two types: virtual damping resistor [21], [22] and control signal shaping. To be specific, the virtual damping resistor is proposed in [21] aiming at equivalently increasing the resistor via control methods while the possible position of the virtual resistor significantly affects the implementation of the control algorithm. The other perspective to achieve active damping by modifying the control signal with compensators includes changing the modulation index in one cycle of the resonance frequency [23], voltage and current feedback control [24] and state feedback control by pole placement approach [27], etc. To synthesis the merits in both categories, a combination of the virtual resistor and control signal shaping is proposed in [23], [25], [26] to achieve better *LC* resonance mitigation. To sum up, these proposed techniques target at suppressing the input AC side *LC* oscillation and alleviating the existed harmonic distortion simultaneously.

When it comes to the modular structure such as MMC in high power applications, the damping resonance is distinct from that in AC-DC converters, since the inherent *RLC* series structure inclines to trigger the transient oscillation in the circulating current and the capacitor voltage at the DC-link side. Aside from that, the second-order circulating current component needs special attention in such topologies. An oscillation suppression method based on active damping is proposed in [29], [30] for MMC based on the small signal state-space model, with which the equivalent parasitic resistance in the arm inductor is increased and the damping ratio is correspondingly enhanced. Reference [31] deals with the *RLC* oscillation issue under the condition of variable frequency operation through closed-loop controlling the circulating current. Whereas, the quantitative relationship between the controller parameter and the damping property remains unclear.

However, the studies in [29]–[31] only focus on the oscillation suppression in a traditional PWM modulated MMC with sinusoidal modulation, where the modulation signal can be readily augmented. These strategies are inapplicable for the MMDCT scenario because the DC transformer typically adopts the square wave modulation for achieving higher DC voltage utilization and smaller lower frequency energy ripples [10], [11]. Therefore, because they do not need to buffer low-frequency power ripples, the specific characteristics of the *RLC* series configuration in MMDCT are more worthy of attention since the submodule capacitors in MMDCT are usually designed smaller than those in traditional MMCs [18], [19]. The smaller submodule capacitance value increases the possibility of oscillation, which seriously threatens the stability of the system. Moreover, the parasitic resistance in the inductance of the phase leg needs to be as small as possible to reduce the system loss, but it will in turn limit the decay rate of oscillation. A dual closed-loop control method in proposed in [32] to cope with the oscillation suppression in a full-bridge back-to-back MMDCT based on '−1/2' modulation. However, the capacitor voltages in each arm should be dynamically sorted to determine which submodule is inserted or bypassed to modify the arm voltage, and the design of the controller parameters is not provided.

Therefore, this paper first analyzes the causes and effects of the transient oscillation phenomenon in MMDCT. Then, the oscillation suppression angle (OSA) is introduced, and its working principle is studied in depth. In addition, the damping ratio of the system with or without OSA is compared by establishing a second-order state space averaging model, which shows the open loop control of OSA is insufficient to improve the system damping. In order to achieve an effective oscillation suppression, a closed-loop control algorithm is adopted, and the gain of the damping compensator is optimally designed to achieve the critical damping state according to the established small-signal model. Besides, the capacitor voltage closed-loop control and the output power control are both established to ensure the stable and safe operation of MMDCT. Comparative simulation results verify the correctness and effectiveness of the proposed transient oscillation suppression method.

II. MATHEMATICAL MODEL AND TRANSIENT OSCILLATION GENERATION MECHANISM OF MMDCT
A. MATHEMATICAL MODEL OF MMDCT
The typical MMDCT topology with medium frequency transformer isolation used for distribution network is depicted in Fig. 1. In the primary side of the transformer a single-phase MMC is used to directly access the high-level DC voltage while in the secondary side a simple and standard H-bridge converter is chosen to provide a low-level DC voltage port. The MMC and the H-bridge converter are connected via a medium frequency (MF) transformer, with the leakage inductor acts as the power exchange media between the primary and secondary side.

In the primary side, the MMC has two phase-legs and each phase-leg incorporates two strings of cascaded half-bridge submodules (SM), namely the MMC arm with *N* SMs, and a coupled arm inductor in between. The two ends
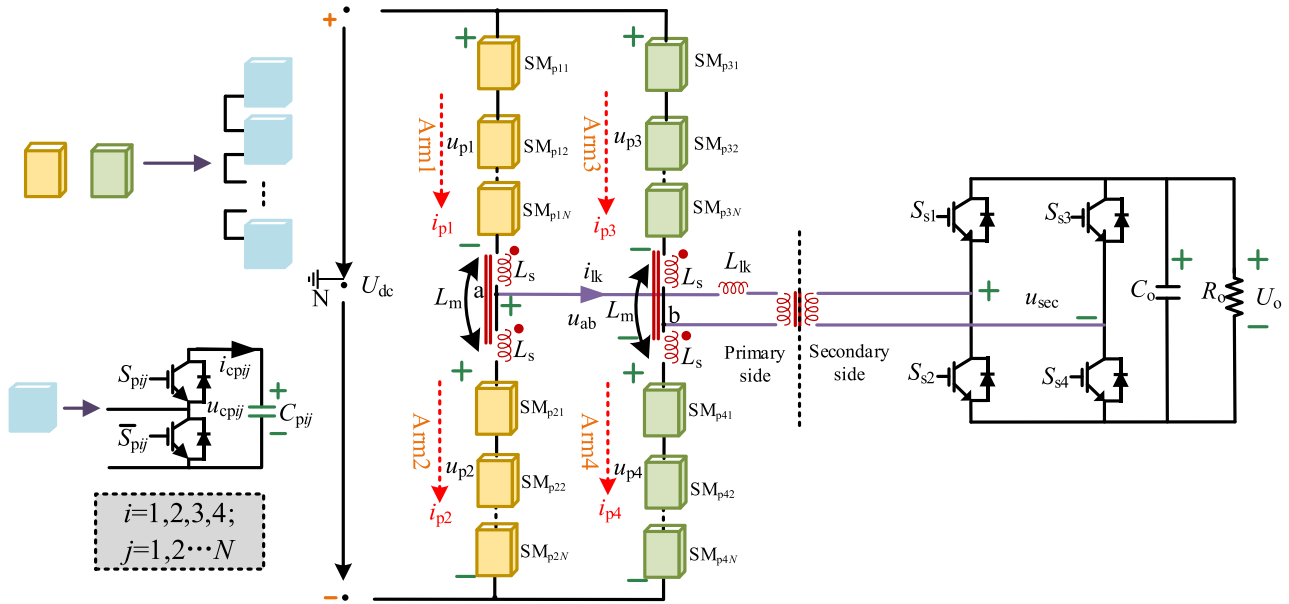
FIGURE 1. Topology of MMDCT used for distribution network.

of the phase-leg form the high-level voltage DC port while the midpoint of the inductor is the high frequency AC port connecting to the primary side of the MF transformer.

On the basis of the MMC operation principles [5], the input DC current is divided equally between two phase-legs and thus form the common-mode or the so-called circulating current that charges the SMs while the differential-mode current is driven identically from both ends of the upper and lower arms to the MF transformer that discharges the SMs and delivers the same amount of power to the secondary side of MMDCT. Taking the phase-leg a of the MMC system-level for instance, Applying Kirchhoff's voltage law to the upper loop (formed by the overall input DC link, the upper arm and the terminal voltage with respect to the neutral point) and the lower loop (formed by the overall input DC link, the lower arm and the terminal voltage with respect to the neutral point), respectively, yields

$$u_{aN} = \frac{1}{2}U_{dc} - u_{p1} - \left(L_s \frac{di_{p1}}{dt} + L_m \frac{di_{p2}}{dt} + i_{p1}R_s \right) \quad (1)$$

$$u_{aN} = -\frac{1}{2}U_{dc} + u_{p2} + \left(L_s \frac{di_{p2}}{dt} + L_m \frac{di_{p1}}{dt} + i_{p2}R_s \right) \quad (2)$$

where U_{dc} and u_{aN} represent the overall input DC voltage and the terminal voltage with respect to the neutral point, respectively; u_{p1}, u_{p2}, i_{p1} and i_{p2} represent the upper and lower arm voltages and currents, respectively; and L_s, L_m and R_s represent the self-inductance, mutual inductance and the inherent parasitic resistance of the coupled arm inductor, respectively.

For simplicity, the aforementioned system current variables can be represented by their common-mode and

differential-mode components as

$$i_{p1} = i_{cma} + i_{dma} \quad (3)$$

$$i_{p2} = i_{cma} - i_{dma} \quad (4)$$

where i_{cma} and i_{dma} represent the common-mode current and the differential-mode current, respectively and i_{dma} is half of the leakage inductor current of the transformer, which is denoted by i_{lk}.

Adding and subtracting (1) and (2) then substituting from (3) and (4) gives

$$\frac{U_{dc}}{2} = \frac{u_{p1} + u_{p2}}{2} + (L_s + L_m) \frac{di_{cma}}{dt} + i_{cma}R_s \quad (5)$$

$$u_{aN} = \frac{-u_{p1} + u_{p2}}{2} - (L_s - L_m) \frac{di_{dma}}{dt} - i_{dma}R_s \quad (6)$$

Note the same conclusion applies for the phase-leg b and the primary side voltage of the MF transformer can be then calculated using the formula $u_{ab} = u_{aN} - u_{bN}$.

On the other hand, the SM-level dynamics are simply described using Ohm's law of capacitor for both upper and lower arms, to give
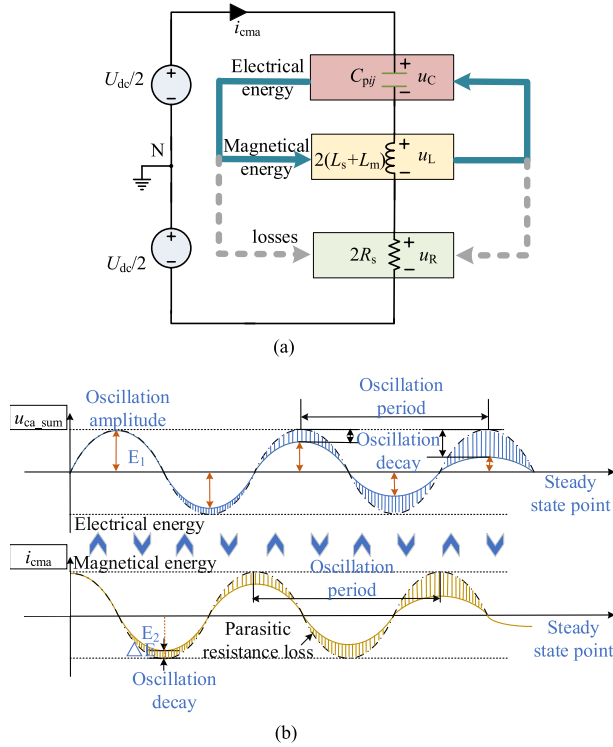
$$i_{cp1j} = C \frac{du_{cp1j}}{dt} \quad (7)$$

$$i_{cp2j} = C \frac{du_{cp2j}}{dt} \quad (8)$$

where u_{cp1j}, i_{cp1j}, u_{cp2j} and i_{cp2j} represent the voltages and charging currents of the jth SM ($j = 1, 2, \ldots N$) in the upper and lower arms, respectively.

B. TRANSIENT OSCILLATION GENERATION MECHANISM OF MMDCT

The common-mode equivalent circuit model of MMDCT is shown in Fig. 2(a), where the SM capacitors are in series with

FIGURE 2. Illustration of the oscillation phenomenon in MMDCT. (a) Form of Energy exchange among the series RLC elements, and (b) Oscillation features of the variables in the time domain.

the arm inductors, so it is susceptible to *LC* oscillations, viz., the capacitor will charge the arm inductor and generate the magnetic energy stored in the inductor coil. After a period of time, the arm inductor will charge the capacitor in a similar manner in order to convert the magnetic energy back into electrical energy. Over and over again, if there is no loss in the series circuit, the energy exchange between the two passive devices will cause continuous and constant oscillation, as shown by the dotted line in Fig. 2(b). However, in reality, the loss in the parasitic resistor of the arm inductor cannot be ignored, so the oscillation amplitude will decay with time, as shown by the solid line in Fig. 2(b). But since the loss is relatively small in a well-designed system, the oscillation attenuation is very slow. That is, the system has insufficient damping. In this case, if the DC voltage or the transmission power command is varied, a significant oscillation of the circulating current and the capacitor voltage inevitably occurs during the transition time.

In order to perform quantitative analysis to verify the oscillation mechanism, the state space equation should be established by selecting the sum of $2N$ submodule capacitor voltages u_{ca_sum} and the circulating current i_{cma} as the corresponding state variables (Assuming the submodule capacitor voltages are well balanced, and thus u_{cp1j} and u_{cp2j} are represented by $u_{ca\_sum}/2N$). Given that the switching ripples of the state variables in a switching period is small (i.e., small ripple approximation [33]), their averaged values during a switching

period are used instead as the actual state variables, to give

$$<u_{ca\_sum}>_{T_s} = \frac{1}{T_s} \int_0^{T_s} u_{ca\_sum}(\tau)d\tau \quad (9)$$

$$<i_{cma}>_{T_s} = \frac{1}{T_s} \int_0^{T_s} i_{cma}(\tau)d\tau \quad (10)$$

where T_s is the switching period and $<u_{ca\_sum}>_{T_s}$ and $<i_{cma}>_{T_s}$ represent the averaged value of $u_{ca\_sum}(t)$ and $i_{cma}(t)$ in each switching period in the phase leg a, respectively.

Based on the traditional 50% square wave modulation [18], the relationship between the system-level and the SM-level voltages and currents are able to be established, as depicted in Fig. 3.
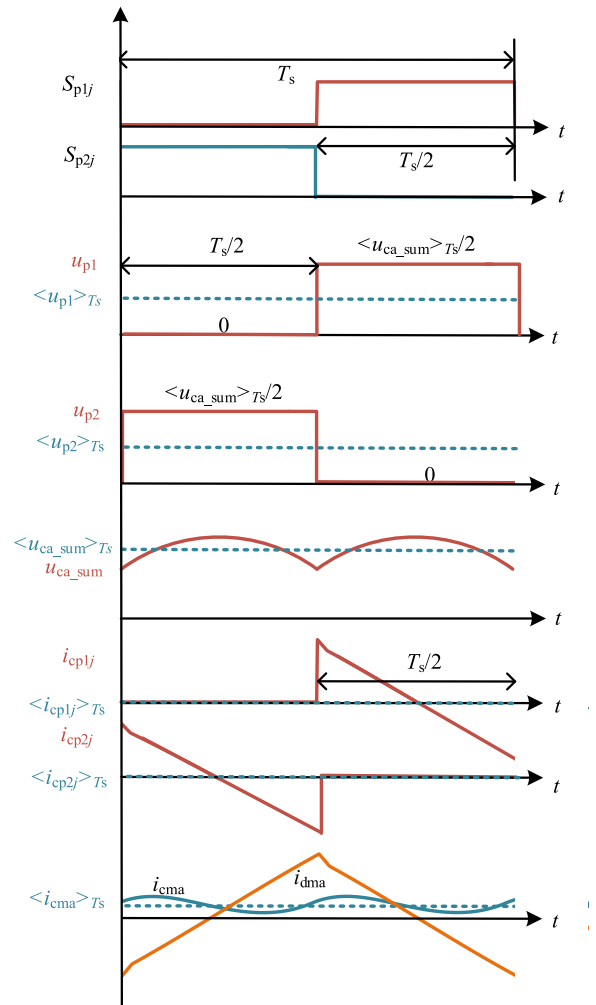
FIGURE 3. Illustration of the averaged state variables with small ripple approximation during a switching period.

1) THE VOLTAGE RELATIONSHIP
Taking the switching signal S_{p1j} in the upper arm as an example, when S_{p1j} is in the 'ON' state the arm output voltage equals to the SM capacitor voltage while when S_{p1j} is 'OFF'

the arm output voltage is 0. The same conclusion applies for the other arms. Therefore, the averaged upper and lower arm voltages $<u_{p1}>_{T_s}$ and $<u_{p2}>_{T_s}$ can be calculated as

$$<u_{p1}>_{T_s} = <u_{p2}>_{T_s} = \frac{1}{4}<u_{ca\_sum}>_{T_s} \quad (11)$$

2) THE CURRENT RELATIONSHIP

Similarly, when S_{p1j} is in the 'ON' state, the SM capacitor current i_{cp1j} equals to the arm current i_1, which can be decomposed into a common-mode current i_{cma} and half a leakage inductor current $i_{lk}/2$. In contrast, when S_{p1j} is in the 'OFF' state, i_{cp1j} is zero. Note that since the leakage inductor current i_{lk} is an AC term varying significantly over a switching period, it is inapplicable for the small ripple approximation. Instead, this current may be averaged by $P/2u_{ab}$, where P denotes the transmitted power in MMDCT and u_{ab} represents the primary side voltage of the transformer, respectively. To further simplify the analysis, this averaged current is approximately seen as a load disturbance, which does not rely on the system state variables, to develop a linear equation. Therefore, u_{ab} approximately equals to $-U_{dc}$ when $S_{p1j} = 1$, and then the capacitor charging current can be calculated as

$$<i_{cp1j}(t)>_{T_s} = <i_{cp2j}(t)>_{T_s} = \frac{1}{2}\left(<i_{cma}(t)>_{T_s} - \frac{P}{2U_{dc}}\right) \quad (12)$$

Substituting (11) and (12) into (5), (7) and (8) yields

$$\frac{d\boldsymbol{x}}{dt} = \begin{pmatrix} 0 & \dfrac{N}{C} \\ -\dfrac{1}{4(L_s + L_m)} & -\dfrac{R_s}{(L_s + L_m)} \end{pmatrix}\boldsymbol{x} + \begin{pmatrix} -\dfrac{NP}{2CU_{dc}} \\ \dfrac{U_{dc}}{2(L_s + L_m)} \end{pmatrix} \quad (13)$$

where $\boldsymbol{x} = [<u_{ca\_sum}(t)>_{T_s}, <i_{cma}(t)>_{T_s}]^T$. By solving the state space matrix in Laplace transformation form in (13), the characteristic roots are readily derived as

$$s_{1,2} = \frac{1}{2}\left(-\frac{R_s}{(L_s + L_m)} \pm \sqrt{-\frac{N}{(L_s + L_m)C} + \frac{R_s^2}{(L_s + L_m)^2}}\right) \quad (14)$$

In general, the system parameters determine that $R_s^2/(L_s + L_m)^2$ is always smaller than $N/(L_s + L_m)C$, hence the system characteristic roots $s_{1,2}$ are a pair of conjugate complex roots with negative real parts, viz.

$$s_{1,2} = -\alpha \pm j\omega_d = -\xi\omega_n \pm j\omega_n\sqrt{1 - \xi^2} \quad (15)$$

where α, ω_d, ξ, ω_n represent the damped oscillation decay rate, the damped oscillation frequency, the damping ratio and the natural oscillation frequency of the MMDCT system, respectively, and are all positive values. From (14) and (15) it is evident that the oscillation phenomenon is associated with the system parameters R_s, L_s, L_m, C and N, where the

damping ratio ξ along with the natural oscillation frequency ω_n can be calculated as

$$\xi = \frac{R_s}{\sqrt{\dfrac{N}{C}(L_s + L_m)}} \quad \omega_n = \sqrt{\frac{N}{4(L_s + L_m)C}} \quad (16)$$
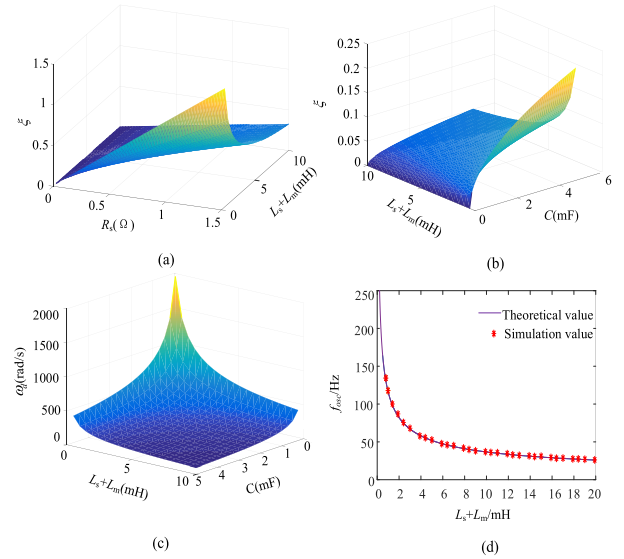
FIGURE 4. The relationship between the physical parameters and the oscillation characteristics. (a) Effect of arm inductance and the parasitic resistance on the damping ratio, (b) Effect of submodule capacitance and arm inductance on the damping ratio, (c) Effect of submodule capacitance and arm inductance on the oscillation frequency, (d) Matching effect of the arm inductance on the oscillation frequency for theoretical calculation and simulation result.

Fig. 4 illustrates how the damping ratio and the oscillation frequency are dependent on the system parameters. When the submodule capacitance C is fixed at 940uF, the damping ratio increases with the increase of the parasitic resistance and the decrease of the arm inductance [see Fig. 4(a)]. It can be seen from Fig. 4(a) that only if the parasitic resistance reaches 1Ω and the arm inductance is smaller than 1mH can the system reaches a satisfactory damping state. Furthermore, when the parasitic resistance is fixed (for example with a typically value of 0.1Ω), the damping ratio will be increased with a smaller arm inductance and larger submodule capacitance [see Fig. 4(b)], but the damping ratio is limited within 0.2 even if the capacitor reaches an unrealistically large value. On the other hand, as depicted in Fig. 4(c) and (d), the oscillation frequency is inversely proportional to the arm inductance and the submodule capacitance while independent of the parasitic resistance.

To sum up, the nature of the MMDCT parameter values indicate the system is liable to suffer from the damped oscillation. Moreover, increasing the damping ratio via changing the physical parameters in MMDCT system is not feasible in practice for the following three reasons: 1) R_s should be designed as small as possible to reduce losses; 2) C does not need to buffer the low frequency energy as a traditional MMC and thus can be selected with a small value to save costs; 3) L_s
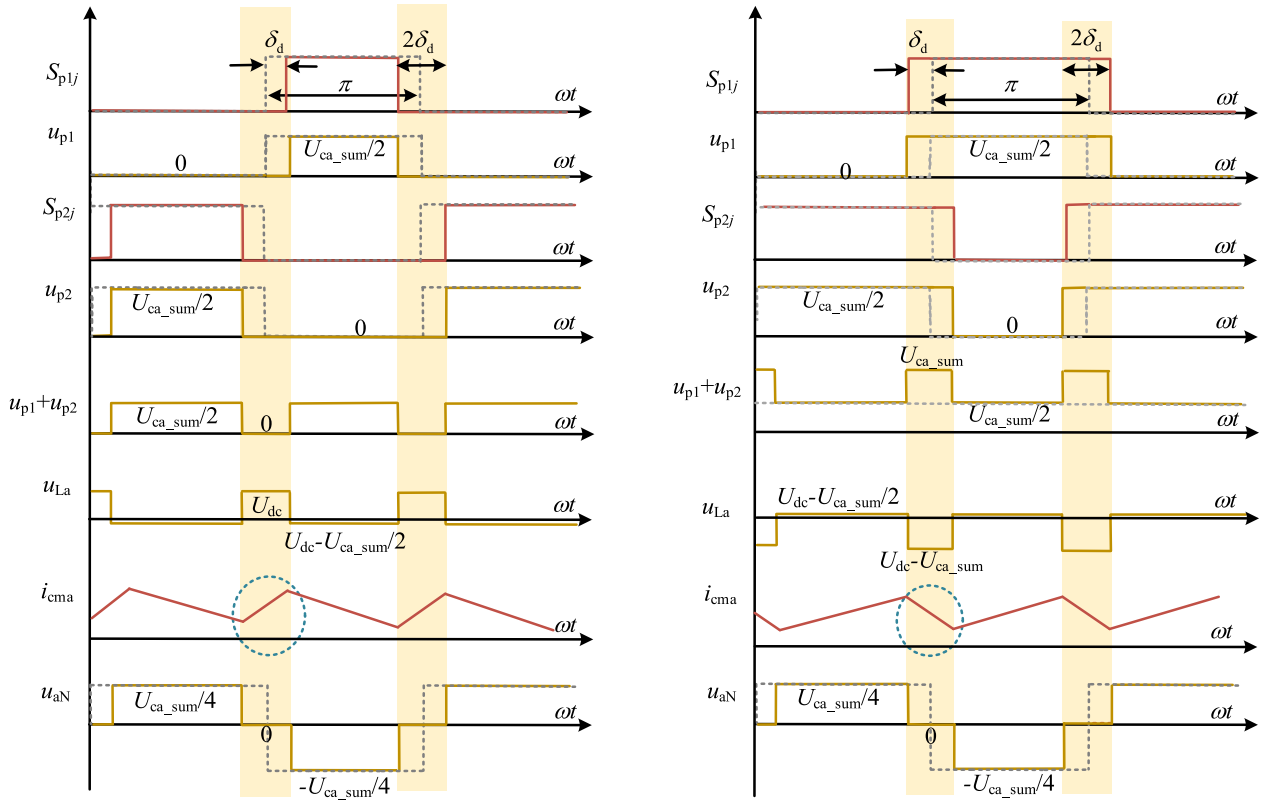
FIGURE 5. Comparison of key variables of MMDCT with and without incorporating the OSA. (a) $\delta_d > 0$; (b) $\delta_d < 0$.

should be larger than a certain value to suppress the possible surge current in the phase leg.

Therefore, it is preferable to increase the system damping by introducing additional control variables under a given system parameter configuration, and thereby an effective control method is to be proposed and detailed in the next section.

III. INCORPORATING AN OSCILLATION SUPPRESSION ANGLE AND ITS EFFECT ON THE SYSTEM DAMPING

An oscillation suppression method is proposed in this section aimed at eliminating the transient oscillation in the circulating current as well as in the capacitor voltages. This method is achieved by incorporating a phase shift angle, which is hereinafter renamed as the oscillation suppression angle (OSA) δ_d, at each edge of the square modulation signals.

A. OPERATING PRINCIPLE OF OSA

Fig. 5(a) and (b) illustrates how the circulating current can be controlled upward and downward through incorporating a positive OSA and a negative OSA, respectively. Their corresponding waveforms are presented with the solid lines in comparison with the waveforms using the conventional 50% square wave modulation with dotted lines. Note the small inter-SM phase shift angles [18] for reducing *dv/dt* stress across the transformer are neglected here for brevity.

When δ_d is positive [see Fig. 5(a)], during the rising edge the driving signals for the upper arm SMs is delayed by δ_d

while during the falling edge is led by δ_d as compared to the traditional 50% square wave modulation. The same principle applies for the lower arm, and thus a zero voltage zone lasting for $2\delta_d$ is generated in $u_{p1} + u_{p2}$. Therefore, the arm inductor voltage u_{La} equals to U_{dc} in this $2\delta_d$ interval that gives rise to the increase in the circulating current.

On the contrary, when a negative δ_d is incorporated, the arm inductor voltage equals to $U_{dc} - U_{ca\_sum}$, which is negative, during the $2\delta_d$ period, and thereby the circulating current is forced decreasing during this period. Note U_{ca_sum} is the value of $<u_{ca\_sum}>_{T_s}$.

To sum up, the incorporation of OSA produces an additional square wave voltage across the arm inductor and its parasitic resistor, which can be controlled positive or negative through choosing a correct polarity of δ_d. As a result, the circulating current is able to be appropriately controlled upward or downward every half switching cycle to suppress the transient oscillation caused by the insufficient damping. Yet, it is desirable to provide quantitative relationship between the enhanced damping ratio and the incorporated OSA.

B. CONTROLLABLE SYSTEM DAMPING RATIO WITH OSA

By incorporating the OSA at both edges of the switching signal, the actual duty cycle of each SM changes from 50% to $(\pi - 2\delta_d)/2\pi$. As a result, the relationship between the system-level and SM-level voltages and currents, as per Fig. 6,
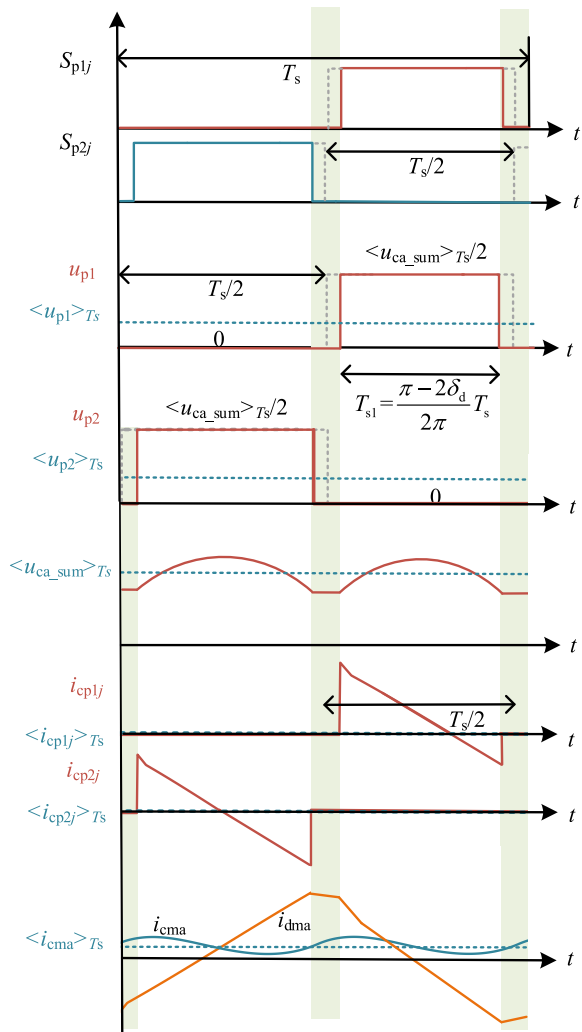
FIGURE 6. Illustration of the averaged state variables during a switching period with the OSA incorporated.

updates to

$$<u_{p1}(t)>_{T_s} = <u_{p2}(t)>_{T_s} = \frac{\pi - 2\delta_d}{4\pi} <u_{ca\_sum}(t)>_{T_s}$$

$$<i_{cp1j}(t)>_{T_s} = <i_{cp2j}(t)>_{T_s}$$
$$= \frac{\pi - 2\delta_d}{2\pi} \left(<i_{cma}(t)>_{T_s} - \frac{P}{2U_{dc}} \right) \quad (17)$$

Then, the averaged state space equation of (13) is rewritten by substituting (17) to into (5), (7) and (8), to give

$$\frac{d\mathbf{x}}{dt} = \begin{pmatrix} 0 & \dfrac{(\pi - 2\delta_d) N}{\pi C} \\ -\dfrac{\pi - 2\delta_d}{4\pi(L_s + L_m)} & -\dfrac{R_s}{(L_s + L_m)} \end{pmatrix} \mathbf{x}$$
$$+ \begin{pmatrix} -\dfrac{(\pi - 2\delta_d) NP}{\pi C U_{dc}} \\ \dfrac{U_{dc}}{2(L_s + L_m)} \end{pmatrix} \quad (18)$$

Similarly as Section II.B, this state-space equation can be solved via calculating the characteristic roots of the state matrix, and then the oscillation decay rate and oscillation frequency are attained as

$$\alpha_\delta = -\frac{R_s}{2(L_s + L_m)}$$

$$\omega_{d\delta} = \frac{\sqrt{\dfrac{N}{C} \dfrac{1}{(L_s + L_m)} \left(\dfrac{\pi - 2\delta_d}{\pi} \right)^2 - \left(\dfrac{R_s}{(L_s + L_m)} \right)^2}}{2} \quad (19)$$

Furthermore, the damping ratio ξ_δ is enhanced due to the introduction of δ_d, which is expressed as

$$\xi_\delta = \frac{R_s}{\dfrac{\pi - 2\delta_d}{\pi} \sqrt{\dfrac{N}{C}} (L_s + L_m)} \quad (20)$$
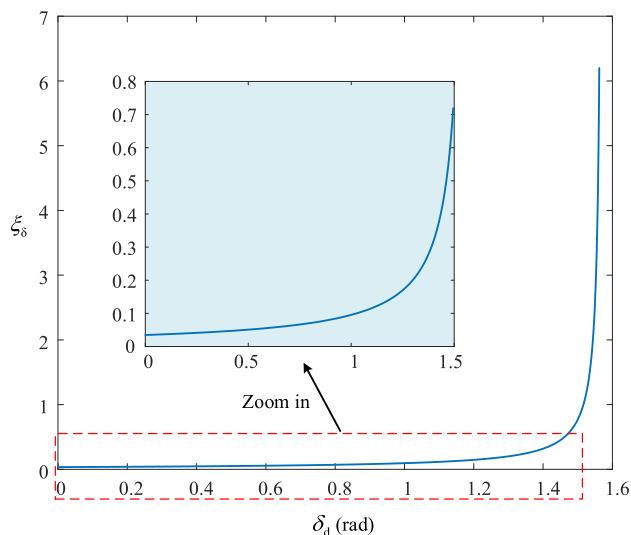

FIGURE 7. Illustration of the effect of the OSA on the damping ratio when $R_s = 100\text{m}\Omega$.

It can be seen from (20) that the damping ratio is controllable owing to the incorporated OSA δ_d. Fig. 7 shows this relationship when R_s is fixed at 100mΩ. Overserving from Fig. 7 reveals that the MMDCT system is extremely underdamped when R_s is small, with the damping ratio smaller than 0.04. By increasing δ_d, only a small growth can be observed in ξ_δ initially, whereas a surge in ξ_δ occurs when δ_d reaches around 1.5 rad.

However, since δ_d is the angle that adjusts the charging/discharging current and maintains the capacitor voltage levels, it is very small in practice. As a result, the introduction of δ_d only provides a possibility to balance the stored power of the system, and it does not assist sufficiently in improving the damping ratio if used in an open loop control manner. Therefore, an active damping method in a closed loop control manner should be implemented to further enhance the system damping, as detailed in the next section.

IV. FURTHER ENHANCING THE SYSTEM DAMPING WITH CLOSED LOOP CONTROL

A. SMALL SIGNAL MODEL AND TRANSFER FUNCTION

In order to further improve the MMDCT system damping and accelerate the oscillation attenuation rate, a closed loop control method for suppressing oscillation is required. Since the mathematical model is nonlinear as per (18) when the OSA δ_d is seen as an input variable, a small signal model that describes the linear relationship between the input signal δ_d and the state variable (seen as the output variable) needs to be developed.

Firstly, the input variable OSA δ_d and the system state variables are perturbed (seen as a DC term plus a small-signal AC term) as below:

$$\begin{cases} \delta_d = \Delta_d + \hat{\delta}_d \\ <u_{ca\_sum}(t)>_{T_s} = U_{ca\_sum} + \hat{u}_{ca\_sum} \\ <i_{cma}(t)>_{T_s} = I_{cma} + \hat{i}_{cma} \end{cases} \quad (21)$$

Then substituting (21) into (18) gives

$$\begin{cases} \dfrac{d\hat{u}_{ca\_sum}}{dt} = \dfrac{N}{C}\dfrac{\pi - 2\left(\Delta_d + \hat{\delta}_d\right)}{\pi} \\ \quad \times \left(\left(I_{cma} + \hat{i}_{cma}\right) - \dfrac{P}{(U_{ca\_sum} + \hat{u}_{ca\_sum})}\right) \\ \dfrac{d\hat{i}_{cma}}{dt} = \dfrac{U_{dc}}{2(L_s + L_m)} - \dfrac{\pi - 2\left(\Delta_d + \hat{\delta}_d\right)}{4\pi(L_s + L_m)} \\ \quad \times \left(U_{ca\_sum} + \hat{u}_{ca\_sum}\right) - \dfrac{R_s}{(L_s + L_m)}\left(I_{cma} + \hat{i}_{cma}\right) \end{cases} \quad (22)$$

Note in (22) the differential-mode current $<i_{dma}>_{T_s}$ is alternatively described by $P/<u_{ca\_sum}>_{T_s}$ to improve the accuracy of the model, since the transmitted power is regulated in a closed-loop form according to the load current variations via the phase shift ratio between the primary and secondary side square wave signals, and thus the current becomes dependent on the capacitor voltage.

The DC term in (22) is the quiescent operating point that matches the steady-state analysis, which is written as follows:

$$\begin{cases} I_{cma} = \dfrac{P}{U_{ca\_sum}} \\ U_{ca\_sum} = \dfrac{2\pi}{\pi - 2\Delta_d}\left(U_{dc} - R_s\dfrac{P}{U_{dc}}\right) \end{cases} \quad (23)$$

It can be seen from (23) that the quiescent OSA value Δ_d is able to be used to adjust the quiescent capacitor voltage U_{ca_sum} to an expected value under a given system working power P. Since the parasitic resistance R_s is relatively small and the reference of U_{ca_sum} is $2U_{dc}$, Δ_d is also very small in practice.

Secondly, by neglecting the DC term and the second-order AC term, Eq. (22) becomes

$$\begin{cases} \dfrac{d\hat{u}_{ca\_sum}}{dt} = \dfrac{N}{C}\left(\dfrac{\pi - 2\Delta_d}{\pi}\right)\left(\hat{i}_{cma} + \dfrac{I_{cma}}{U_{ca\_sum}}\hat{u}_{ca\_sum}\right) \\ \dfrac{d\hat{i}_{cma}}{dt} = -\dfrac{\pi - 2\Delta_d}{4\pi(L_s + L_m)}\hat{u}_{ca\_sum} + \dfrac{\hat{\delta}_d}{2\pi(L_s + L_m)}U_{ca\_sum} \\ \quad - \dfrac{R_s}{(L_s + L_m)}\hat{i}_{cma} \end{cases} \quad (24)$$

Finally, by transforming (24) into the Laplace form, the control-to-output transfer function can be then derived as

$$\begin{aligned} G_{i\delta}(s) &= \dfrac{\hat{i}_{cma}(s)}{\hat{\delta}_d(s)} \\ &= \dfrac{\dfrac{U_{ca\_sum}}{2\pi(L_s + L_m)}\left(s - \dfrac{\pi - 2\Delta_d}{\pi}\dfrac{NI_{cma}}{CU_{ca\_sum}}\right)}{s^2 + Ms + O} \end{aligned} \quad (25)$$

where M and O are specified as

$$\begin{aligned} M &= -\dfrac{\pi - 2\Delta_d}{\pi}\dfrac{NI_{cma}}{CU_{ca\_sum}} + \dfrac{R_s}{(L_s + L_m)} \\ O &= \dfrac{\pi - 2\Delta_d}{\pi}\dfrac{N}{(L_s + L_m)C}\left(\dfrac{\pi - 2\Delta_d}{4\pi} - \dfrac{I_{cma}R_s}{U_{ca\_sum}}\right) \end{aligned} \quad (26)$$
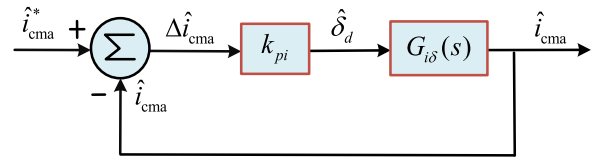
FIGURE 8. Illustration of the s-domain small signal block diagram of the damping compensator.

B. DESIGN OF DAMPING COMPENSATOR

A damping compensator using a proportional controller that is effective in improving the system damping ratio is depicted in Fig. 8. Through solving the characteristic equation $1 + k_{pi}G_{i\delta}(s) = 0$, the characteristic roots can be calculated as

$$s_{1,2} = \dfrac{-M' \pm j\sqrt{4O' - (M')^2}}{2} = -\alpha \pm j\omega_d \quad (27)$$

where M' and O' are specified as

$$\begin{aligned} M' &= M + \dfrac{U_{ca\_sum}}{2\pi(L_s + L_m)}k_{pi} \\ O' &= O - \dfrac{(\pi - 2\Delta_d)NI_{cma}}{2\pi^2(L_s + L_m)C}k_{pi} \end{aligned} \quad (28)$$

It can be seen from (28) that by incorporating a positive gain k_{pi} the oscillation amplitude decays faster and the oscillation frequency becomes lower as compared to the open loop control system with fixed Δ_d. As a result, the damping ratio $\xi_{k\Delta}$ further updates to

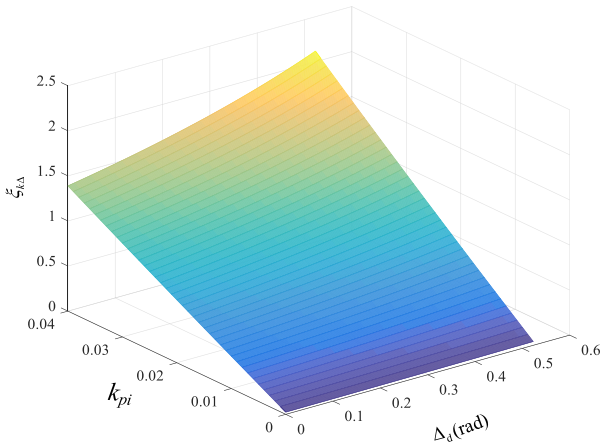$$\xi_{k\Delta} = \dfrac{M'}{2\sqrt{O'}} \quad (29)$$

FIGURE 9. The augmented damping ratio influenced by the damping compensator gain and the OSA.

FIGURE 10. Simulation waveforms of circulating current under different damping compensation methods. (a) Without damping compensation, (b) With open loop damping compensation, (c) Closed loop damping compensation with non-ideal compensator gain, (d) Closed loop damping compensation with the optimum compensator gain.

Combining (23) with (29), the variation of $\xi_{k\Delta}$ depending on that of k_{pi} and δ_d is illustrated in Fig. 9. It is clear from Fig. 9 that the MMDCT system can be easily adjusted to the critical damping state with the regulation of k_{pi}, at a given steady-state operating point of Δ_d, in comparison with the open loop control of i_{cma} with a fixed Δ_d.

The specific performance of the damped oscillation with different damping compensator gains k_{pi} at a fixed Δ_d (selected as 0.002rad) is listed in Table 1. It can be seen from the table that the oscillation decay rate along with the damping ratio increases significantly as expected with a small increase in k_{pi} while the oscillation frequency keeps decreasing with the increase of k_{pi}. When k_{pi} reaches 0.029 the MMDCT system reaches the critical damping state with the oscillation frequency decays to zero. Note the critical damping state with lower bandwidth is preferable in this case rather than the industrially suggested damping ratio of 0.707.

Theoretical calculation of the precise k_{pi} is by setting $\xi_{k\Delta} = 1$ in (29), to give

$$k_{pi} = \frac{2\pi(L_s + L_m)\left(2\sqrt{O'} - M'\right)}{U_{ca\_sum}} \quad (30)$$

It is worth noting that the optimal k_{pi} is dependent on the system steady-state operating point, which may vary under different load/power conditions, and thus the damping compensator gain should be adjusted in a self-adaptive manner to guarantee a satisfactory dynamic response, particularly under large load step up/down scenarios.

Fig. 10 provides a comparison of the circulating current dynamic response without and with utilizing damping compensation methods. Fig. 10(a) depicts the circulating current waveform without using any damping compensation strategy in which a significant oscillation occurs during the transient period. When the open loop damping compensation method with a fixed OSA is incorporated, the damping ratio remains the same response [see Fig. 10(b)] which is in consistent with
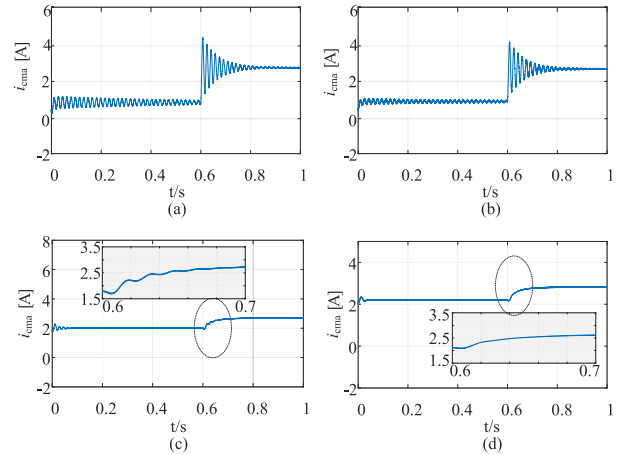
TABLE 1. The characteristics of the damped oscillation with different damping compensator gains.

k_{pi}	α	ω_d	$\xi_{k\Delta}$
0.0001	10.36	368.64	0.0281
0.001	21.38	367.94	0.0580
0.004	58.11	363.21	0.1581
0.007	94.84	354.63	0.2585
0.010	131.56	341.92	0.3593
0.013	168.29	324.58	0.4606
0.016	205.02	301.83	0.5622
0.019	241.75	272.31	0.6643
0.022	278.48	233.46	0.7668
0.025	315.20	179.32	0.8697
0.028	351.93	84.34	0.9731
0.0285	358.05	51.73	0.9904
0.029	364.18	--------	1.0076
0.030	376.42	--------	1.0422

the conclusion in Section III. In contrast, the damping compensation with closed loop control of OSA presents significant improvement in the dynamic response [see Fig. 10(c) and (d)]. Note that the damping oscillation in i_{cma} still exists for 0.1s when the damping compensator gain k_{pi} is not optimally designed [see Fig. 10(c)].
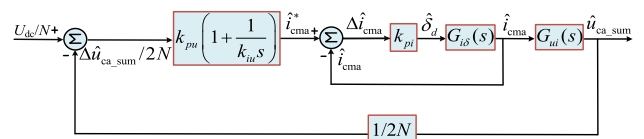

FIGURE 11. Illustration of the s-domain small-signal block diagram of the primary side of MMDCT.

Additionally, the SM capacitor voltage control using a PI regulator is typically required to provide a circulating current

reference, as illustrated in Fig. 11, as well as to balance the input and output power. The controller parameters k_{pu} and k_{iu} are set according to offline design using MATLAB, where the current-to-voltage transfer function $G_{ui}(s)$ is derived from (24), as below

$$G_{ui}(s) = \frac{N\,(\pi - 2\Delta_d)}{\pi\,C\left(s - \frac{\pi - 2\Delta_d}{\pi}\,\frac{NI_{cma}}{CU_{ca\_sum}}\right)} \quad (31)$$

(a)

(b)
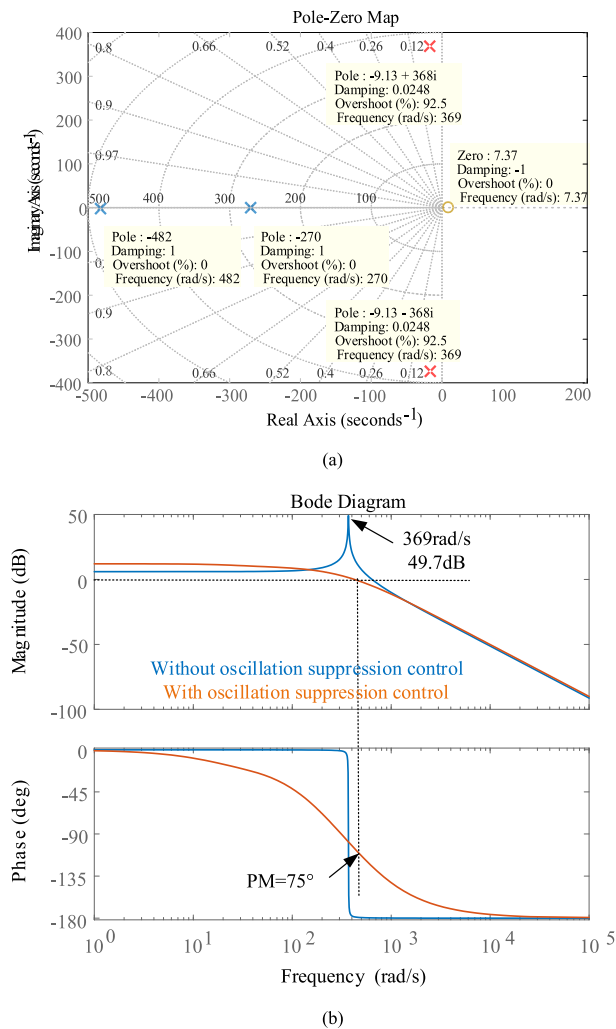
FIGURE 12. Stability analysis of the proposed oscillation suppression control method. (a) Zeroes and poles of the inner circulating current loop when k_{pi} varies, (b) bode plot of the system without and with the dual loop control method.

C. STABILITY ANALYSIS

The stability of the inner current loop and the outer voltage loop is verified in Fig. 12(a) and Fig. 12(b), respectively. In Fig. 12(a), a pair of conjugate complex roots with negative real part appear in the MMDCT system without using any damping compensation method, in which case the frequency is 369rad/s and the damping ratio is 0.0248. In contrast, the roots evolve into two distinct negative real values with

TABLE 2. Simulation parameters.

Parameters	Values
DC bus voltage (U_{dc})	4kV
Number of cells per arm (N)	8
Switching frequency (f_s)	1kHz
Turns ratio of saturated transformer (n)	16:3
Saturation characteristic(A, H)	(0.6,1)(60,0.08)
Winding inductance and resistance(Ω, mH)	0.06, 0.2
Arm coupled inductor (L_s)	2mH
Secondary side voltage (U_o)	750V
SM capacitor/load capacitor (C_{pij}, C_o)	940uF
Load resistance (R_o)	2.5Ω, 5Ω

the damping ratio compensated to 1 (i.e., with k_{pi} calculated in (30)). Note that there is a positive zero in both cases, which may adversely affect the dynamic process of the system.

The stability of the overall dual loop control system is shown in Fig. 12(b), where the resonant peak reaches as high as 49.7dB at the frequency of 369rad/s. With adjusting the PI regulator, the resonance is completely eliminated with a phase margin of 75 deg. This makes sure the overall voltage control loop reaches a satisfactory damping state, and no oscillation will appear in the capacitor voltages during transient period.
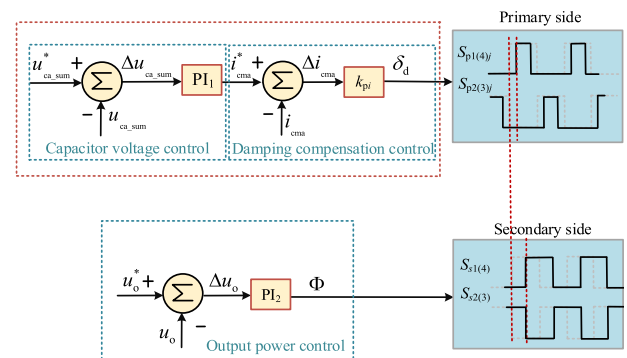

FIGURE 13. The overall control diagram of MMDCT.

D. THE OVERALL CLOSED LOOP CONTROL SYSTEM OF MMDCT

The overall control diagram of the MMDCT system is given in Fig. 13. Apart from the dual loop control in the primary side, an outer phase shift angle Φ undertakes the role of adjusting the active power transfer between the primary and secondary side of MMDCT, in order to fulfill the assumption made in (22) that the transmitted power is the disturbance relying solely on the load while the differential-mode current depends on the capacitor voltages. Hence the output voltage is closed-loop controlled with a PI regulator to track the load power demand.

V. SIMULATION VERIFICATION

The feasibility and effectiveness of the proposed transient oscillation suppression method has been investigated in PSIM, with the system configuration and parameters listed

in Table 2. In order to better compare the effects without and with using the proposed damping compensation method, the underdamped oscillation is designed to be more significant with the parasitic resistance of the phase leg set to a small value ($R_s = 10\text{m}\Omega$). In order to perform the simulation in a more practical way, the quasi-two level modulation is adopted here to reduce dv/dt. Furthermore, results using the saturated medium-frequency transformer are compared to that from a traditional linear transformer.
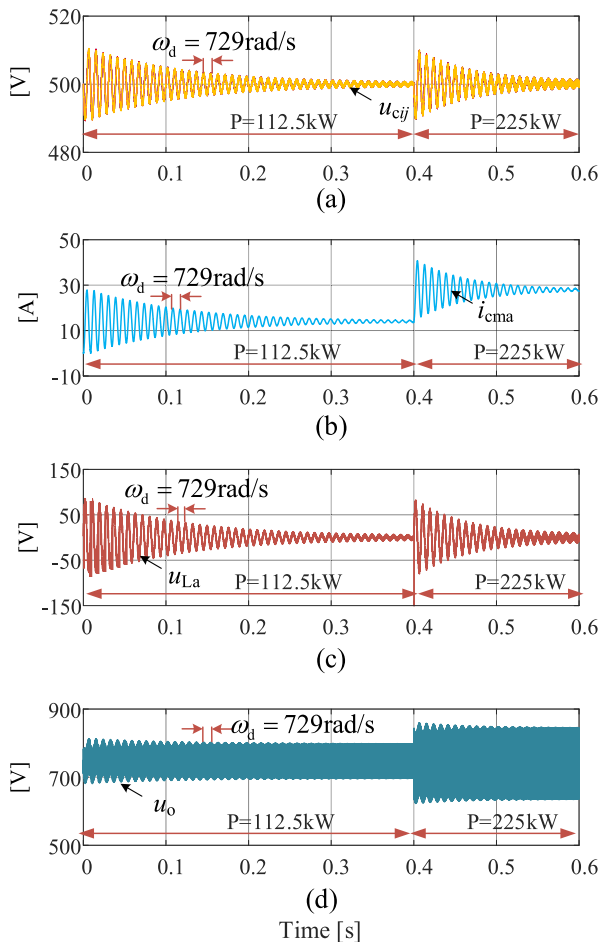
FIGURE 14. Transient performance of MMDCT without the proposed oscillation suppression control method. (a) Capacitor voltages, (b) Circulating current, (c) Arm inductor voltage, (d) Output voltage.

A. TRANSIENT RESPONSE RESULTS WITHOUT USING THE PROPOSED CONTROL METHOD

The transient response of the system, including the submodule capacitor voltages u_{cij}, the circulating current i_{cma}, the arm inductor voltage u_{La} and the output side voltage u_o, without using any damping compensation method is illustrated in Fig. 14, where a load power step increase from 112.5kW to 225kW is triggered at $t = 0.4$ s. All these variables present significant oscillation phenomenon, demonstrating that the original MMDCT system is underdamped as explained in Section II. Note the oscillation frequency

is around 729 rad/s that is consistent with the theoretical analysis in (16), verifying the correctness of the quantitative analysis of the oscillation mechanism. Since the decay rate of the transient oscillation correlates to the product of ξ and ω_n, the oscillation will disappear after a long time if there is no load change. However, since the disturbance is inevitable in the MMDCT system, the MMDCT system is likely to oscillate frequently, threatening the safe operation of the system.

Moreover, the load transient at $t = 0.4$s triggers much more serious oscillations in the aforementioned variables with higher resonance peak value. In summary, both steady-state response and transient response are undesirable without using any damping compensation method in MMDCT system, indicating the necessity of incorporating the proposed control method to suppress the transient oscillation in a second-order system.

### B. TRANSIENT RESPONSE RESULTS WITH CLOSED LOOP CONTROL OF OSA

The transient response of i_{cma} and δ_d during load step up/down using a single circulating current control loop are depicted in Fig. 15. When the load power steps down [refer to Fig. 15] from 225kW to 112.5kW at $t = 0.6$s, the circulating current reference decreases suddenly, and then the actual circulating current is larger than the new target value during the transient process. As a result, δ_d is adjusted negative to produce an overlapped gating signals [refer to S_{p1j}, S_{p2j} in Fig. 15], whose duty ratio increases to $(\pi - \delta_d)/2\pi$, because of which the circulating current will decrease in the $2\delta_d$ period to track the new reference. Eventually, i_{cma} will be stable around the new reference after several switching periods and δ_d will return to its stable operation point as well.

On the other hand, when the load power steps up [refer to Fig. 16] from 112.5kW to 225kW at $t = 0.6$s, the actual circulating current will be smaller than the new reference, that is, δ_d will be controlled positive to provide a $2\delta_d$ zone for i_{cma} to increase until it reaches the new reference, with the duty ratio of S_{p1j} and S_{p2j} being decreased to $(\pi - \delta_d)/2\pi$. Note that there is relatively larger ripple current in i_{cma} during the start-up transient procedure, which is on account of the larger difference between the actual current and the reference and thus δ_d is adjusted larger to provide a relatively longer rising/falling time in the circulating current. With i_{cma} approaching the steady-state value, the value of δ_d turns back smaller, giving rise to smaller ripple in the current.

Note that the operation mechanism of OSA is to modify the duty ratio of the 180° phase shifted signals in each switching pair (S_{p1j} and S_{p2j}), while the inner submodule phase shift angel θ in the quasi-two level modulation changes the phase shift angle among N submodules per arm with the 180° phase shift characteristic maintained between S_{p1j} and S_{p2j}. In other words, the incorporation of θ will not affect the feasibility of OSA, while it only affects the moment when each switching pair acts on the circulating current.
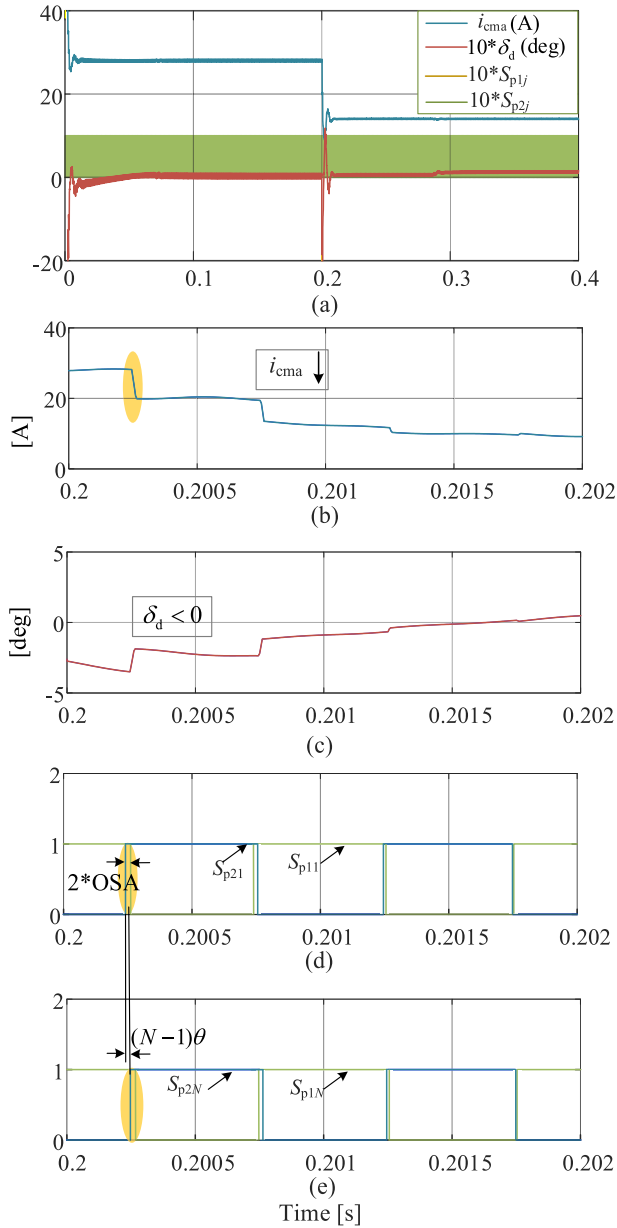
FIGURE 15. Simulation waveforms of the load transient response for verifying the operation mechanism of δ_d adjusted by circulating current loop control. (a) Load power step down, (b) Zoom of i_{cma}, (c) Zoom of δ_d, (d) Zoom of S_{p11} and S_{p21}. (e) Zoom of S_{p1N} and S_{p2N}.
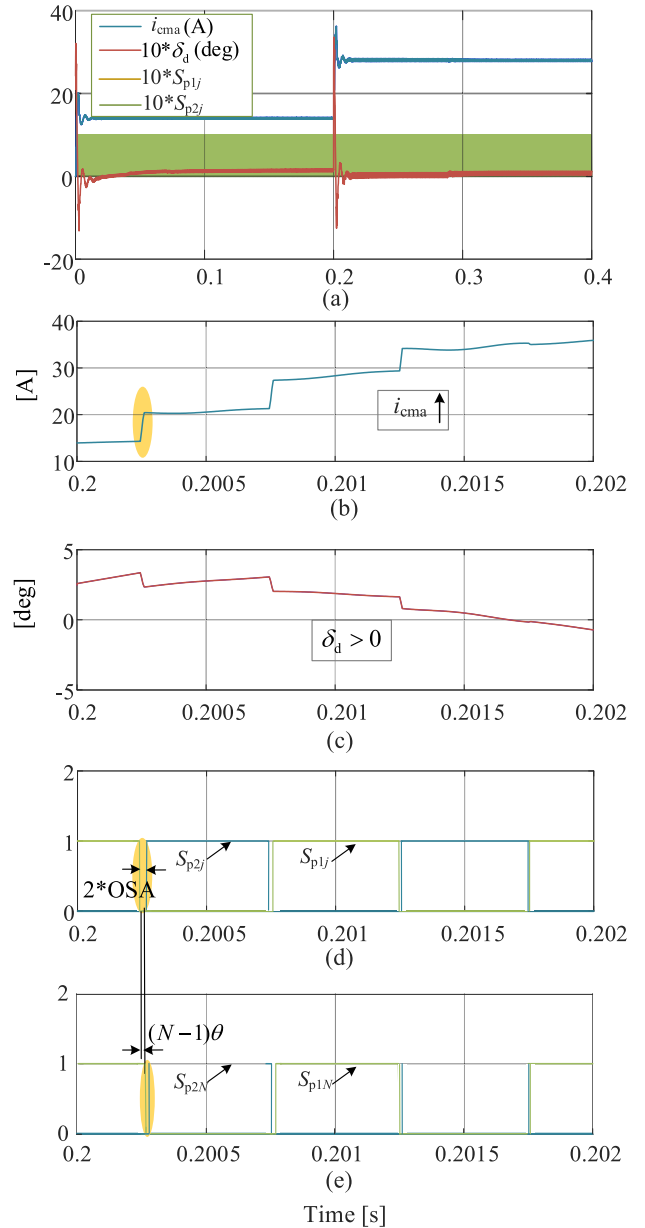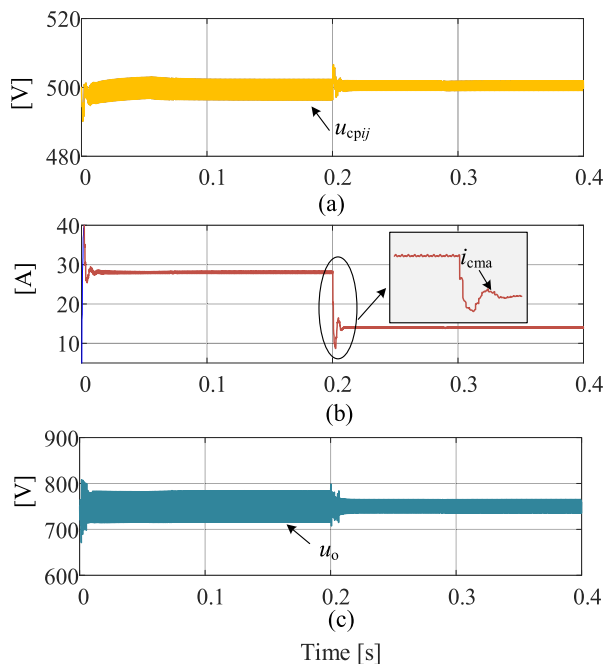

FIGURE 16. Simulation waveforms of the load transient response for verifying the operation mechanism of δ_d adjusted by circulating current loop control. (a) Load power step up, (b) Zoom of i_{cma}, (c) Zoom of δ_d, (d) Zoom of S_{p11} and S_{p21}. (e) Zoom of S_{p1N} and S_{p2N}.

## C. THE OVERALL TRANSIENT RESPONSE RESULTS WITH THE PROPOSED CONTROL METHOD

A load power step-up transient response from $P = 112.5$kW to $P = 225$kW and a step-down transient response from $P = 225$kW to $P = 112.5$kW are both provided to verify the effectiveness of the proposed closed-loop oscillation suppression control method, as depicted in Fig. 17 and Fig. 18, respectively. Both steady-state and transient response are satisfactory without evident oscillations, thus the damping characteristics and the stability of MMDCT system get improved sufficiently. This is achieved with the optimal controller gain

designed to compensate the system to the critical damping state.

Hence, the pulse voltage with the duty ratio of δ_d/π is generated across the arm inductor with the closed-loop control of the circulating current, and accordingly the transformer primary side voltage augments to three level where the zero level lasts for $2\delta_d$. To be specific, if the actual circulating current is larger than the desired value, a negative perturbation will be overlaid on the steady state operating point of Δ_d to reduce the increment of i_{cma} as compared to the previous switching period and vice versa, back and forth, the circulating current

FIGURE 17. Simulation waveforms of load step down (P = 225kW to P = 112.5kW) when R_s = 0.01Ω with the proposed transient oscillation suppression method. (a) Submodule capacitor voltages, (b) Circulating current, (c) Output voltage.
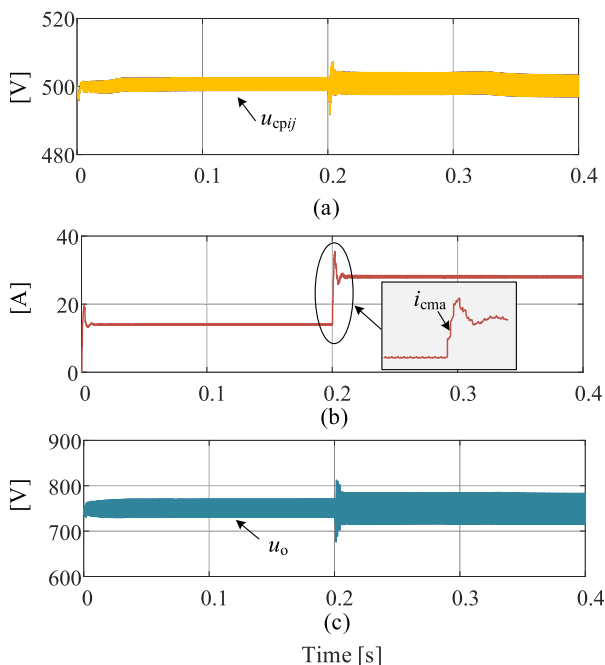
FIGURE 18. Simulation waveforms of load step up (P = 112.5kW to P = 225kW) when R_s = 0.01Ω with the proposed transient oscillation suppression method. (a) Submodule capacitor voltages, (b) Circulating current, (c) Output voltage.

will be adjusted around the reference and the oscillation in i_{cma} will be completely suppressed as well as that in u_{cpij}, u_{La} and u_o, without imposing any burden into the system losses.

In addition, the outer capacitor voltage control provides the reference of the circulating current and eliminates the steady state error in capacitor voltages effectively. Besides, the output voltage is well maintained to the reference of 750V via the output power closed loop control with only 4% voltage drop during transient process. Thereby, a desirable stability state of a MMDCT system is achieved with critical damping ratio though sacrificing the dynamic response to some extent.
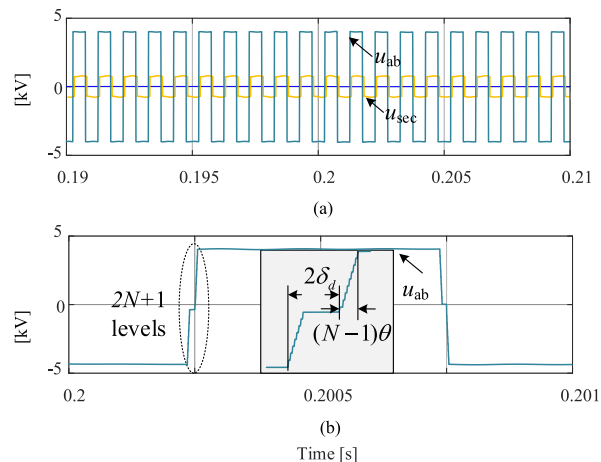
FIGURE 19. Simulation waveforms of the transformer voltages with the proposed transient oscillation suppression method during transient process. (a) Primary side voltage u_{ab} and secondary side voltage u_{sec}, (b) Zoom of u_{ab}.
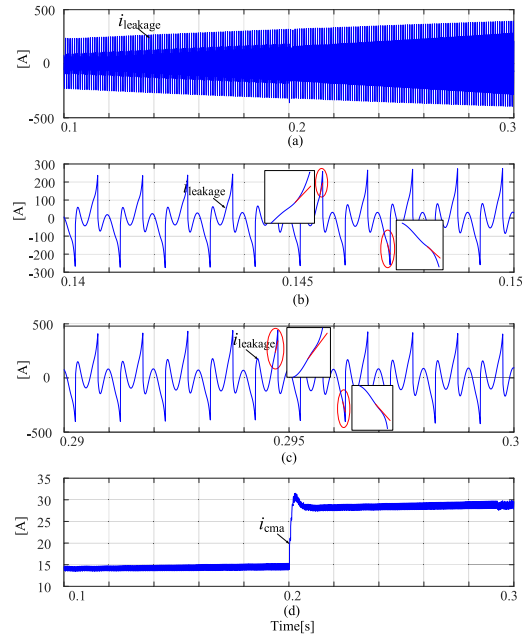
Besides, the outer phase shift angle Φ between the primary and secondary side increases (relatively small due to the input DC link voltage is large) under the circumstance of the load power transient to adjust the transmitted power through the transformer, as depicted in Fig. 19. Since the quasi-two level modulation is adopted to limit dv/dt where the inter SM phase shift angle $\theta = 0.1\%\pi$, the overlapped zone in the N switching signal pairs are generated by OSA and phase shifted sequentially by θ, hence the primary side voltage u_{ab} has $2N + 1$ levels during the falling and rising edges, as depicted in Fig. 20. Nevertheless, it only lasts for a short period of $(2*OSA + (N - 1)\theta)$ since OSA is around $1\%\pi$ during the transient process and zero during the steady state and θ is also small enough. Therefore, the introduced OSA and θ will not contribute to the saturation of the medium-frequency transformer in MMDCT.

In order to investigate the validity of the proposed transient oscillation suppression method using a saturable transformer, simulation waveforms are compared in Fig. 21 and Fig. 22. When the piecewise linear relationship between the flux Φ and magnetizing current i_m satisfies ($3.75*10^{-4}$Wb, 0.6A)($3*10^{-3}$Wb, 60A), the transformer will be saturated since the maximum flux Φ_{max} determined by $\Phi - i_m$ curve equals to 0.003Wb (much smaller than Φ_m = 0.04Wb solved in equation $U = 4.44fN\Phi_m$, where U is the effective value of U_{dc}), hence the primary side transformer current $i_{leakage}$ keeps increasing with a sharply increased slope introduced, as shown in the zoomed view of the red circle of Fig. 21. When $\Phi - i_m$ curve satisfies (0.0375Wb, 0.6A)(0.3Wb, 60A),
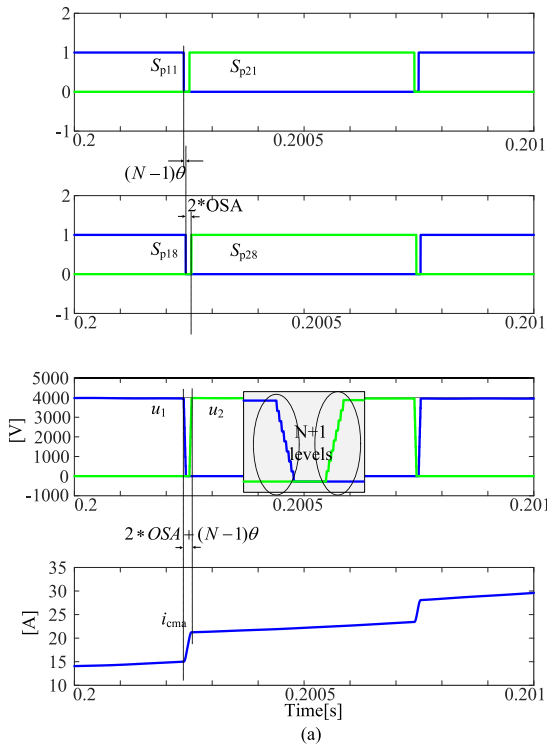
FIGURE 20. Simulation waveforms of transient response under the proposed oscillation suppression method when quasi two level modulation is added (2*OSA < θ). (a) Load step up, (b) Load step down.

FIGURE 21. Validity of the proposed transient oscillation suppression method when the transformer is saturated. (a) Transformer primary side current, (b) Zoom of (a) when t ∈ [0.14s,0.15s], (c) Zoom of (a) when t ∈ [0.29s,0.3s], (d) Circulating current i_{cma}.
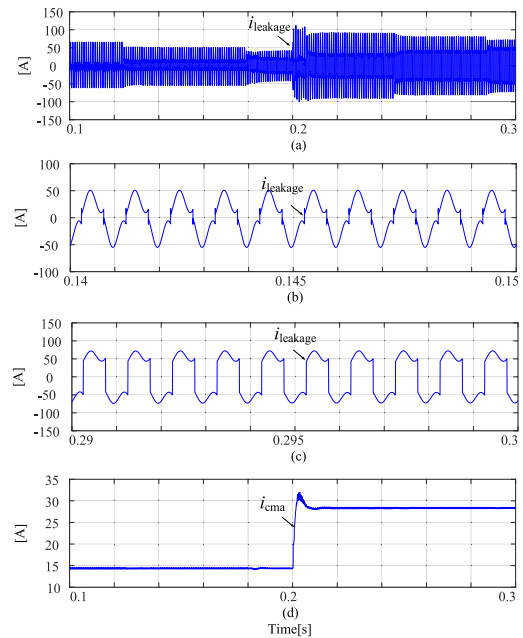
FIGURE 22. Validity of the proposed transient oscillation suppression method when the transformer is not saturated. (a) Transformer primary side current, (b) Zoom of (a) when t ∈ [0.14s,0.15s], (c) Zoom of (a) when t ∈ [0.29s,0.3s], (d) Circulating current i_{cma}.

the maximum flux Φ_{max} equals to 0.3Wb and the transformer will not suffer from saturation so the primary side current in transformer is stable, as shown in Fig. 22. Note that when the transformer is saturated, the circulating current shows divergence while the oscillation in the circulating current is

suppressed with the proposed transient oscillation suppression control method. When the transformer is not saturated, the circulating current is stable with no transient oscillation phenomenon. Hence, the circulating current is well regulated without any oscillation no matter the transformer is saturated or not, and the proposed transient oscillation method is of validity.

VI. CONCLUSION

The study in this paper shows that MMDCT has a low-frequency oscillation problem due to the small value of the submodule capacitance, which is more likely to occur than the traditional MMC. By introducing an OSA designed to adjust the direction of change in the circulating current, it is able to improve the system damping and suppress the transient oscillation. Through the small-signal linearization of the established second-order state space model, the transfer function of OSA-to-current is derived, and the improved damping ratio of the MMDCT system with closed-loop control of OSA is achieved. Simulation results from an industrial-level MMDCT model in PSIM validate the effectiveness of the proposed OSA along with the damping compensator control approach.

REFERENCES

[1] M. Tabari and A. Yazdani, "Stability of a DC distribution system for power system integration of plug-in hybrid electric vehicles," *IEEE Trans. Smart Grid*, vol. 5, no. 5, pp. 2564–2573, Sep. 2014.

[2] B. Zhao, Q. Song, J. Li, W. Liu, G. Liu, and Y. Zhao, "High-frequency-link DC transformer based on switched capacitor for medium-voltage DC power distribution application," *IEEE Trans. Power Electron.*, vol. 31, no. 7, pp. 4766–4777, Jul. 2016.

[3] B. Zhao, Q. Song, W. Liu, and Y. Sun, "Overview of dual-active-bridge isolated bidirectional DC–DC converter for high-frequency-link power-conversion system," *IEEE Trans. Power Electron.*, vol. 29, no. 8, pp. 4091–4106, Aug. 2014.

[4] G. G. Oggier, G. O. Garcia, and A. R. Oliva, "Modulation strategy to operate the dual active bridge DC-DC converter under soft switching in the whole operating range," *IEEE Trans. Power Electron.*, vol. 26, no. 4, pp. 1228–1236, Apr. 2011.

[5] Y. Sun, C. A. Teixeira, D. G. Holmes, B. P. McGrath, and J. Zhao, "Low-order circulating current suppression of PWM-based modular multilevel converters using DC-link voltage compensation," *IEEE Trans. Power Electron.*, vol. 33, no. 1, pp. 210–225, Jan. 2018.

[6] Y. Sun, D. Lyu, C. A. Teixeira, B. P. McGrath, D. G. Holmes, and Q. Wang, "Circulating current suppression control of modular multilevel converters under optimized phase disposition (PD) modulation," in *Proc. IEEE Energy Convers. Congr. Expo. (ECCE)*, Baltimore, MD, USA, Sep. 2019, pp. 201–208.

[7] D. Lyu, Y. Sun, C. A. Teixeira, Z. Ji, J. Zhao, and Q. Wang, "A modular multilevel dual buck inverter with adjustable discontinuous modulation," *IEEE Access*, vol. 8, pp. 31693–31709, 2020.

[8] D. Lyu, Y. Sun, C. A. Teixeira, D. G. Holmes, B. P. McGrath, and Q. Wang, "A novel modular multilevel converter with coupled-inductor semi-bridge submodules," in *Proc. IEEE Energy Convers. Congr. Expo. (ECCE)*, Baltimore, MD, USA, Sep. 2019, pp. 6860–6867.

[9] L. Harnefors, S. Norrga, A. Antonopoulos, and H. Nee, "Dynamic modeling of modular multilevel converters," in *Proc. EPE*, Birmingham, U.K., 2011, pp. 1–10.

[10] C. Sun, X. Cai, G. Shi, and J. Zhang, "Voltage balancing control of isolated modular multilevel DC–DC converter for use in DC grids with zero voltage switching," *IET Power Electron.*, vol. 9, no. 2, pp. 270–280, Feb. 2016.

[11] Z. Wang, J. Zhang, and K. Sheng, "An isolated bidirectional modular multilevel DC/DC converter for power electronic transformer applications," *J. Power Electron.*, vol. 16, no. 3, pp. 861–871, May 2016.

[12] Y. Shi, R. Li, Y. Xue, and H. Li, "Optimized operation of current-fed dual active bridge DC–DC converter for PV applications," *IEEE Trans. Ind. Electron.*, vol. 62, no. 11, pp. 6986–6995, Nov. 2015.

[13] J. Huang, Y. Wang, Z. Li, and W. Lei, "Unified triple-phase-shift control to minimize current stress and achieve full soft-switching of isolated bidirectional DC–DC converter," *IEEE Trans. Ind. Electron.*, vol. 63, no. 7, pp. 4169–4179, Jul. 2016.

[14] T. T. Song, N. Huang, and A. Ioinovici, "A zero-voltage and zero-current switching three-level DC–DC converter with reduced rectifier voltage stress and soft-switching-oriented optimized design," *IEEE Trans. Power Electron.*, vol. 21, no. 5, pp. 1204–1212, Sep. 2006.

[15] O. M. Hebala, A. A. Aboushady, K. H. Ahmed, and I. Abdelsalam, "Generic closed-loop controller for power regulation in dual active bridge DC–DC converter with current stress minimization," *IEEE Trans. Ind. Electron.*, vol. 66, no. 6, pp. 4468–4478, Jun. 2019.

[16] N. Hou, W. Song, Y. Zhu, X. Sun, and W. Li, "Dynamic and static performance optimization of dual active bridge DC-DC converters," *J. Mod. Power Syst. Clean Energy*, vol. 6, no. 3, pp. 607–618, May 2018.

[17] B. Zhao, Q. Song, W. Liu, and W. Sun, "Current-stress-optimized switching strategy of isolated bidirectional DC–DC converter with dual-phase-shift control," *IEEE Trans. Ind. Electron.*, vol. 60, no. 10, pp. 4458–4467, Oct. 2013.

[18] C. Sun, X. Cai, J. Zhang, and G. Shi, "Suppression of reactive power in isolated modular multilevel DC–DC converter under quasi square-wave modulation," *IEEE Access*, vol. 7, pp. 23940–23950, 2019.

[19] R. Mo, H. Li, and Y. Shi, "A phase-shifted square wave modulation (PS-SWM) for modular multilevel converter (MMC) and DC transformer for medium voltage applications," *IEEE Trans. Power Electron.*, vol. 34, no. 7, pp. 6004–6008, Jul. 2019.

[20] G. Franklin, J. Powell, and A. Emami, "Dynamic response," in *Feedback Control of Dynamic Systems*, 6th ed. New York, NY, USA: Prentice-Hall, 2005, pp. 444–476.

[21] P. A. Dahono, "A method to damp oscillations on the input LC filter of current-type AC-DC PWM converters by using a virtual resistor," in *Proc. IEEE INTELEC*, Yokohama, Japan, 2003, pp. 757–761.

[22] K. Jaitrong, S. Phonsri, and M. Kupimai, "A modify technique to actively damp oscillation in the input LC filter of three-phase PWM rectifier," in *Proc. 5th Int. Conf. Electr. Eng./Electron., Comput., Telecommun. Inf. Technol.*, Krabi, Thailand, May 2008, pp. 1017–1020.

[23] Y. Neba, "A simple method for suppression of resonance oscillation in PWM current source converter," *IEEE Trans. Power Electron.*, vol. 20, no. 1, pp. 132–139, Jan. 2005.

[24] Z. Bai, H. Ma, D. Xu, B. Wu, Y. Fang, and Y. Yao, "Resonance damping and harmonic suppression for grid-connected current-source converter," *IEEE Trans. Ind. Electron.*, vol. 61, no. 7, pp. 3146–3154, Jul. 2014.

[25] Z. Shuai, H. Cheng, J. Xu, C. Shen, Y. Hong, and Y. Li, "A notch filter-based active damping control method for low-frequency oscillation suppression in train–network interaction systems," *IEEE J. Emerg. Sel. Topics Power Electron.*, vol. 7, no. 4, pp. 2417–2427, Dec. 2019.

[26] Y. Xiao, Z. Wang, S. You, M. Cheng, and L. Xu, "Active damping of LC resonance for paralleled indirect matrix converter based on cascaded control," in *Proc. IEEE Energy Convers. Congr. Expo. (ECCE)*, Milwaukee, WI, USA, Sep. 2016, pp. 1–8.

[27] V. R. Chowdhury, S. Mukherjee, P. Shamsi, and M. Ferdowsi, "State feedback control to damp output LC filter resonance for field oriented control of VSI fed induction motor drives," in *Proc. 9th Annu. IEEE Green Technol. Conf. (GreenTech)*, Denver, CO, USA, Mar. 2017, pp. 370–375.

[28] N. Zhao, G. Wang, D. Xu, and D. Xiao, "An active damping control method for reduced DC-link capacitance IPMSM drives," *IEEE Trans. Ind. Electron.*, vol. 65, no. 3, pp. 2057–2068, Mar. 2018.

[29] Q. Xu, A. Luo, F. Ma, Q. Xiong, and L. Wang, "Circulating current suppressing method based on active damping control of MMC considering low-frequency oscillation," *Trans. China Electrotech. Soc.*, vol. 30, no. 24, pp. 118–126, Dec. 2015.

[30] Y. Yue, Q. Xu, Z. Shuai, Z. He, P. Guo, Y. Li, A. Luo, and J. Shen, "Low-frequency harmonic resonance analysis and suppression method of modular multilevel converter," *IET Power Electron.*, vol. 11, no. 4, pp. 755–763, Apr. 2018.

[31] J. Pan, Z. Ke, R. Na, M. Al Sabbagh, J. Zhang, J. Wang, and L. Xu, "Circulating current resonant oscillation in modular multilevel converters for variable frequency operation and its suppression method," in *Proc. IEEE Energy Convers. Congr. Expo. (ECCE)*, Portland, OR, USA, Sep. 2018, pp. 686–692.

[32] H. Zhao, R. Li, X. Li, X. Cai, Y. Shi, and H. Li, "A novel modulation strategy for isolated modular multilevel DC/DC converter's sub-module DC voltage oscillation damping," in *Proc. IEEE 8th Int. Power Electron. Motion Control Conf. (IPEMC-ECCE Asia)*, Hefei, China, May 2016, pp. 47–52.

[33] R. W. Erickson and D. Maksimovic, "AC equivalent circuit modeling," in *Fundamentals of Power Electronics*, 2nd ed. New York, NY, USA: Springer, 2001, pp. 213–226.

DAN LYU (Graduate Student Member, IEEE) received the B.S. degree in electrical engineering from Nanjing Normal University, Nanjing, China, in 2018, where she is currently pursuing the master's degree with the School of Electrical and Automation Engineering. Her current research interests include the modulation and control of power electronic converters, with a particular emphasis on multilevel converters.

YICHAO SUN (Member, IEEE) received the B.S. and Ph.D. degrees in electrical engineering from Southeast University, Nanjing, China, in 2010 and 2017, respectively.

From February 2015 to August 2016, he was a Visiting Scholar with the Power Electronics Group, RMIT University, Melbourne, Vic., Australia. Since 2017, he has been with the School of Electrical and Automation Engineering, Nanjing Normal University, Nanjing, where he is currently a Lecturer. He has published over 20 conference and journal articles and has coauthored two international patents. His current research interests include the modulation and control of power electronic converters, with a particular emphasis on multilevel converters. He received the Third Best Paper Award, in IEEE IECON, 2013.

YUFAN LI received the B.S. degree in electrical engineering from the Nanjing Institute of Technology, Nanjing, China, in 2019. He is currently pursuing the master's degree with the School of Electrical and Automation Engineering, Nanjing Normal University. His current research interests include the modulation and control of power electronic converters, with a particular emphasis on multilevel converters.

JIANFENG ZHAO received the B.S. degree from Huainan Mining Institute, Huainan, China, in 1995, the M.S. degree from the Nanjing University of Aeronautics and Astronautics, Nanjing, China, in 1998, and the Ph.D. degree from Southeast University, Nanjing, in 2001, all in electrical engineering.

In 2001, he joined the Faculty of the School of Electrical Engineering, Southeast University, where he has been a Professor and has been engaged in teaching and research in the field of high power electronics since 2008. Since 2014, he has also been serving as the Dean with the School of Electrical Engineering, Southeast University. He has published more than 100 technical articles. He holds more than 20 China patents. His main research interests include utility applications of power electronics in smart grid such as, solid-state transformer, active filters for power conditioning, flexible ac-transmission system devices, multilevel ac-motor drives, and efficient energy utilization. He has been a member of the Technical Committee on standard voltages, current ratings and frequencies of China since 2010 and the All-China Youth Federation since 2010.

ZHENDONG JI received the B.S. and Ph.D. degrees in electrical engineering from Southeast University, Nanjing, China, in 2007 and 2015, respectively.

Since 2015, he has been with the School of Automation, Nanjing University of Science and Technology, Nanjing, where he is currently a Lecturer. His main research interests include cascade multilevel converters and solid-state transformers.

DONGYE LI (Member, IEEE) received the B.S. degree from Nanjing Normal University, Nanjing, China, in 2009, and the M.S. and Ph.D. degrees in electrical engineering from Southeast University, Nanjing, in 2013 and 2019, respectively.

Since 2019, he has been with the School of Electric Power Engineering, Nanjing Institute of Technology, Nanjing, where he is currently a Lecturer. His current research interests include cascade multilevel converters, modular multilevel converters, and power electronic transformers.

• • •